Hyperspectral LSFM with DMD-only shaping and neural network reconstruction

Sébastien Crombez, Cedric Ray Garreau, Chloé Exbrayat-Heritier, Florence Ruggiero, Nicolas Ducros

To cite this version:

Sébastien Crombez, Cedric Ray Garreau, Chloé Exbrayat-Heritier, Florence Ruggiero, Nicolas Ducros. Hyperspectral LSFM with DMD-only shaping and neural network reconstruction. Optics Express, 2025, 33 (25), pp.52339-52355. ⟨10.1364/OE.570091⟩. ⟨hal-04824372v2⟩

HAL Id: hal-04824372

https://hal.science/hal-04824372v2

Submitted on 22 Jul 2025

Hyperspectral LSFM with DMD-only Shaping and Neural Network Reconstruction

SÉBASTIEN CROMBEZ[1,2], CÉDRIC RAY[1,2], CHLOÉ EXBRAYAT-HÉRITIER[3], FLORENCE RUGGIERO[3], NICOLAS DUCROS[1,4,*]

[*] *nicolas.ducros@creatis.insa-lyon.fr*
[1] *INSA-Lyon, Université Claude Bernard Lyon 1, CNRS, Inserm, CREATIS UMR 5220, U1294, F-69621, LYON, France*
[2] *Université Claude Bernard Lyon 1, CNRS, Institut Lumière Matière, F-69622, Villeurbanne, France*
[3] *Institut de Génomique Fonctionnelle de Lyon, ENS-Lyon, UMR CNRS 5242, Universite Claude Bernard Lyon 1, Lyon Cedex, France*
[4] *Institut Universitaire de France, France*

Abstract: Quantitative fluorescence imaging in biological samples with autofluorescence or spectrally overlapping fluorophores remains a challenge for conventional light sheet fluorescence microscopy (LSFM). To address this, we introduce DNR-HLSFM, a novel approach for hyperspectral LSFM (HLSFM) that is based on DMD-only light shaping and Neural network Reconstruction (DNR). This computational technique combines structured illumination with a physical model of the acquisition process, a denoising neural network and non negative unmixing, to enable robust fluorophore quantification. DNR-HLSFM does not rely on optical filters, which overcomes limitations in spectral resolution and signal loss. We experimentally demonstrate our method by imaging zebrafish embryos in three dimensions, achieving effective autofluorescence removal and precise separation of two spectrally overlapping red fluorophores. This work may pave the way for versatile, high-resolution, quantitative hyperspectral imaging in biomedical research, significantly expanding the capabilities of LSFM. To promote reproducibility and foster further development, we have made our raw data, reconstructed data and code publicly available.

1. Introduction

Light sheet fluorescence microscopy (LSFM) has revolutionized 3D imaging of biological samples, offering low photobleaching, high acquisition speeds, and deep penetration [1–3]. Its ability to capture dynamic processes in living specimens has made it indispensable in developmental and cell biology [4–6]. However, conventional filter-based LSFM suffers from limitations in quantitative analysis, particularly in samples with autofluorescence or multiple fluorophores with overlapping emission spectra [7].

Hyperspectral imaging, which measures light spectra across hundreds of channels, has addressed similar challenges in other fields [8]. While hyperspectral LSFM has been explored [9–16], existing approaches often rely on complex hardware or compromise spatial/spectral resolution. Furthermore, phasor-based methods assume simplified spectral models [17]. Recent advances in computational imaging, driven by compressed sensing [18] and deep learning for inverse problems [19–22] offer new possibilities. Computational hyperspectral imaging acquires hypercubes from few measurements, leveraging data-driven algorithms for improved image reconstruction speed and quality [23–25]. The field of computational hyperspectral imaging is moving very fast with the advent of deep learning [26]. Many novel techniques have emerged in the last few years with application to video imaging [27,28], lensless imaging [29], miniaturized spectroscopy [30], spectral imaging using metasurfaces [31], to cite only a few.

In this work, we introduce DNR-HLSFM, a novel approach for hyperspectral LSFM (HLSFM) that is based on DMD-only light shaping and Neural network Reconstruction (DNR). Inspired by single-pixel imaging [27,32–35] and Hadamard transform optics [36], our method uses a digital micromirror device (DMD) that generates light sheets spatially modulated along the dimension orthogonal to the slit of the spectrograph, recovering the orthogonal dimension via a data-driven algorithm. One of the main motivations behind our work is the superiority of Hadamard multiplexing over push-broom acquisition, often referred to as Fellgett's advantage [37]. This advantage was extensively studied in the 1970s [36] and more recently [38]. In contrast to the approach described in [14], we use a DMD alone to shape the structured light sheets, which significantly improves the modulation and leads to a 3.5-fold improvement in spatial resolution in the transverse direction. Moreover, our algorithm integrates a physical model of the structured illumination with a denoising neural network trained in a supervised manner, which demonstrates robust reconstruction at varying light intensities. Furthermore, we incorporate spectral unmixing to quantify individual fluorophores. Our experimental system for DNR-HLSFM supports both conventional and hyperspectral imaging, demonstrating its effectiveness in zebrafish embryos by removing auto-fluorescence and separating DsRed and mRFP, two red fluorescent proteins with overlapping emission spectra. This work should expand application of LSFM to previously difficult to image samples and opens new avenues in biomedical research, such as the analysis of complex biological processes or the enhancement of the accuracy in drug discovery and toxicology studies.

2. Imaging principle

2.1. Structured light sheet

Conventional LSFM illuminates the sample from the side with a uniform sheet of light [39]. In contrast, our hyperspectral approach is based on structured sheets that are modulated along the dimension orthogonal to the propagation axis (see Fig. 1b). We achieve the structured sheets by illuminating a DMD with a Gaussian beam. We then focus the light using a lens (see L in Fig. 1b) and an illumination objective (see O1 in Fig. 1b). A diaphragm must be placed at the focal point of the lens (see D Fig. 1b) to filter out the diffraction pattern created by the DMD. The generation of the structured light sheet is computer-controlled by uploading appropriate spatial patterns onto the DMD (see Fig. 1c). The optical layout of our DNR-HLSFM device is provided in Section 1 of Supplementary document.

The transverse modulation of the sheet is controlled by the transverse modulation of the DMD pattern, while its thickness is controlled by the height of the DMD pattern. Great care must be taken to cope with diffraction. We retain only the zero-th diffraction order to maximise the illumination uniformity along the optical axis (see Section 2 of Supplementary document). While previous attempts to combine a cylindrical lens with a DMD resulted in a bulky system with low spatial frequency modulation [14], our DMD-only approach is compact and demonstrates improved spatial resolution. Our system produces sharp optical sectioning, generating 1.5×1.5 mm^2 structured sheets whose thickness can be computer-controlled down to 8 µm (FWHM, see Section 3 of Supplementary document). Using 128 modulation patterns, sharp transverse modulations are produced that translate into a transverse resolution of 16 µm for a longitudinal resolution of 7 µm (see Section 4.1). Compared to [14], this represents a 3.5× improvement in the resolution in the transverse direction.

Hadamard modulation profiles were chosen to benefit from Fellgett's advantage, gained from the acquisition of multiplexed rather than direct measurements [40]. Fellgett's advantage is demonstrated by comparing the images obtained with our setup using Hadamard illuminations and line (i.e., push-broom) illuminations. Over the range 500–600 nm, we observe an improvement in the peak signal-to-noise ratio of 7-8 dB (see Section 4.3).

2.2. Double arm set-up

The fluorescence emitted within the light sheet passes through the collection objective and is sent to either a grayscale or spectral arm (see Fig. 1a). The grayscale arm corresponds to conventional

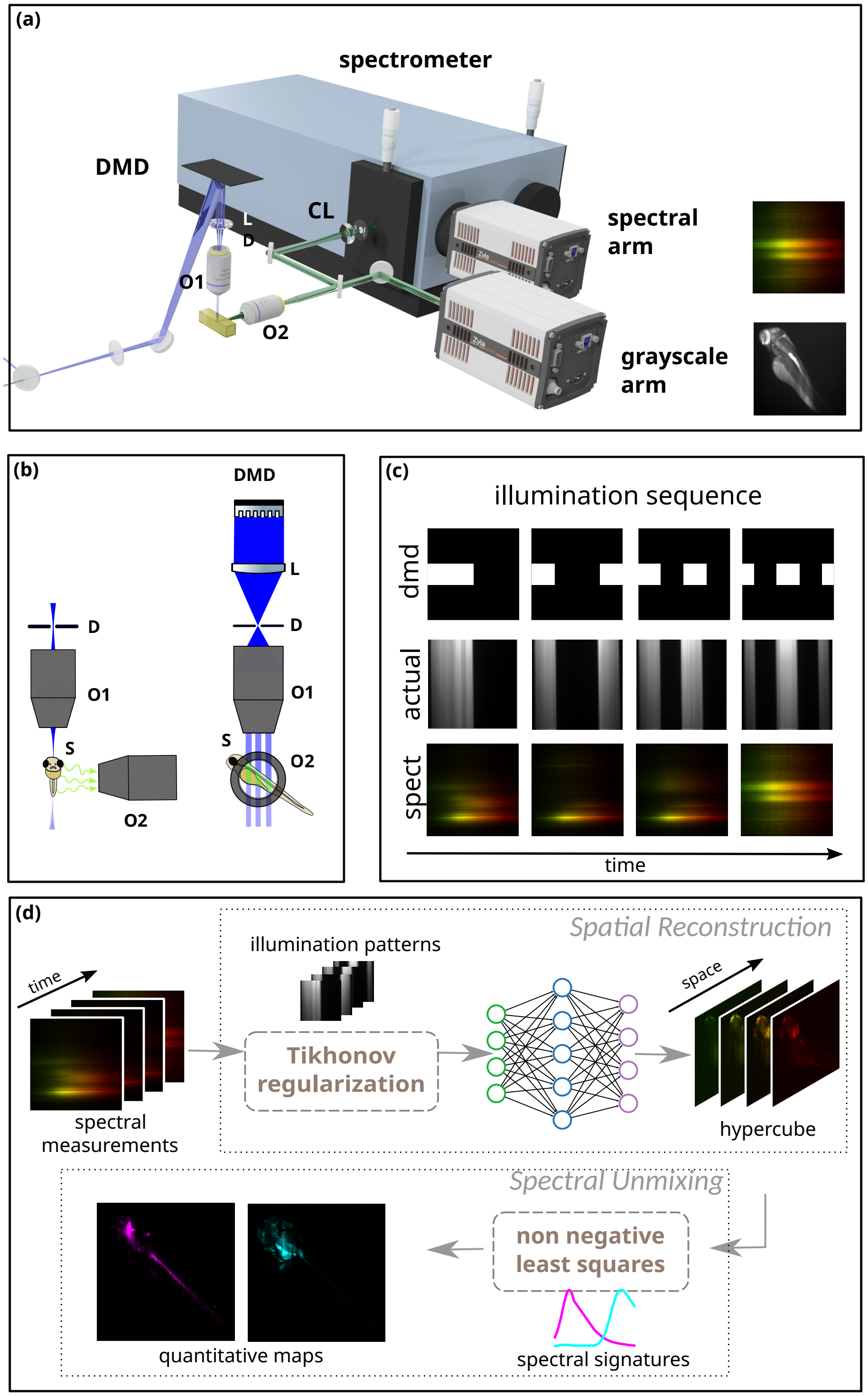

Fig. 1. Overview of DNR-HLSFM. **a**, Fluorescence from the illuminated sheet is focused onto the entrance slit of an imaging spectrometer (spectral arm); the same signal can also be imaged directly by camera (grayscale arm). **b**, To recover the spatial dimension orthogonal to the slit, which is lost during acquisition, the illumination sheet is modulated transversally using a DMD. CL: cylindrical lens; D: diaphragm; DMD: digital micromirror device; L: lens; O1 and O2: objectives; S: sample. **c**, A sequence of measurements is acquired by the spectral arm by uploading several modulation patterns onto the DMD. **d**, The hypercube is recovered from the sequence of spectral measurements by a data-driven reconstruction algorithm that combines knowledge of the actual illumination patterns, Tikhonov regularisation and a convolutional neural network. Given the spectral signature of the components of the specimen, a non-negative least squares unmixing algorithm then quantifies the concentration of the fluorescent proteins of interest.

LSFM, where a camera acquires the fluorescence distribution across the two spatial dimensions of the illumination plane. When a sample with homogeneously distributed fluorescence is considered, the grayscale arm acquires the distribution of light within the illumination plane, which corresponds to the actual illumination profile and differs from the profile uploaded onto the DMD (see Fig. 1c). The grayscale arm is therefore capable of both conventional LSFM and calibration of the modulation profiles of the structured light sheets. Knowledge of the actual illumination profiles is a critical aspect of the reconstruction algorithm.

In the spectral arm, an objective followed by a cylindrical lens focus the light originating from the imaging plane onto the entrance slit of imaging spectrometer. Therefore, the spectral camera acquires multiple spectra along the entrance slit that correspond to integrals of the fluorescence distribution in the transverse direction (Fig. 1c). The transverse spatial dimension lost during the acquisition process can be recovered by exploiting several spectra acquired using several illumination profiles as described in Section 3. We consider a Czerny-Turner spectrometer with a 300 line/mm grating leading to a spectral resolution of 2 nm across a bandwidth of 108 nm.

3. Two-step algorithm for reconstruction and unmixing

We recover the quantitative abundance maps of fluorophores using the two-step algorithm depicted in Fig. 1d and detailed below. The first step reconstructs the transverse spatial dimension lost during acquisition, while the second step unmixes the multiple spectral components (e.g., fluorophores) of the hypercube, leading to quantitative abundance maps.

3.1. Acquisition model

The measurements in DNR-HLSFM acquisitions originate from both the spatial mixing induced by the imaging device (see Eq. (1)) and the spectral mixing inherent to the sample (see Eq. (2) models). The measurements are modelled as

$$\boldsymbol{M}_\lambda = \boldsymbol{H}\boldsymbol{F}_\lambda + \boldsymbol{E} \quad, 1 \leq \lambda \leq \Lambda, \tag{1}$$

where $\boldsymbol{H} \in \mathbb{R}^{K\times N_x}$ represents the measurement matrix that concatenates the K spatial light profiles used for acquisition, $\boldsymbol{F}_\lambda \in \mathbb{R}^{N_x\times N_y}$ is a λ-slice of the full hypercube, and $\boldsymbol{E} \in \mathbb{R}^{K\times N_y}$ represents the measurement errors. The spatial light profiles of our device are determined experimentally (see Fig. 1c; more details provided in Section 3 of Supplementary document; see also Fig. S6 of Supplementary document). We denote by $\boldsymbol{F} = [\mathsf{vec}\,(F_1)\,,\dots,\mathsf{vec}\,(F_\Lambda)]^\top \in \mathbb{R}^{\Lambda\times N}$, $N = N_xN_y$, the full hypercube arranged in matrix form by concatenating all λ-slices, representing the total number of pixels.

Assuming that the sample is made of Q distinct spectral components, the full hypercube can be modelled as

$$\boldsymbol{F} = \boldsymbol{S}\boldsymbol{A}, \tag{2}$$

where $\boldsymbol{S} \in \mathbb{R}^{\Lambda\times Q}$ represents the spectral signatures of the components, and $\boldsymbol{A} \in \mathbb{R}^{Q\times N}$ represents the quantitative abundance of each spectral component per pixel. In the case of fluorescent imaging, a component can represent either a single specific fluorophore (e.g., EGFP, DsRed or mRFP) or a combination of fluorophores (e.g., autofluorescence).

3.2. Image-domain approach

Our goal is to recover the quantitative abundance maps $\boldsymbol{A}$ from the measurements $\boldsymbol{M}_\lambda$, $1 \leq \lambda \leq \Lambda$, knowing the measurement matrix $\boldsymbol{H}$ and assuming prior knowledge about the spectral signatures $\boldsymbol{S}$. To do so, we adopt an image-domain approach that involves spatial reconstruction followed by spectral unmixing that has been found in single-pixel imaging to be more efficient and suitable than spectral unmixing before spatial reconstruction [41].

We first recover the full hypercube $\boldsymbol{F}$ (spatial reconstruction) before recovering the quantitative abundance maps $\boldsymbol{A}$ (spectral unmixing), as described below and illustrated in Fig. 1.

- Step 1 (spatial reconstruction): Recover the λ-slice $\boldsymbol{F}_\lambda$ from the measurement $\boldsymbol{M}_\lambda$, for all spectral channels $1 \leq \lambda \leq \Lambda$, given the measurement matrix $\boldsymbol{H}$. This corresponds to the inversion of Eq. (1).
- Step 2 (spectral unmixing): Recover the quantitative abundance maps $\boldsymbol{A}$ from the full hypercube $\boldsymbol{F}$ calculted in step 1, given the spectral signatures $\boldsymbol{S}$. This corresponds to the inversion of Eq. (2).

3.3. Spatial reconstruction: Tikhonov-Net

We reconstruct the λ-slices using the Tikhonov-Net, a two-step reconstruction network of the form

$$\mathcal{R}_\theta = \mathcal{G}_\theta \circ \mathcal{R}, \tag{3}$$

where $\mathcal{G}_\theta : \mathbb{R}^{N_x \times N_y} \to \mathbb{R}^{N_x \times N_y}$ is a neural network with parameters θ acting in the spatial domain (e.g., a convolutional network), $\mathcal{R} : \mathbb{R}^{K \times N_y} \to \mathbb{R}^{N_x \times N_y}$ is a mapping from the measurement domain to the spatial domain, and $\circ$ represents function composition. Our goal is to reconstruct all the λ-slices using the same reconstruction network, despite the different λ-slices have different signal-to-noise ratios. Inspired by [42], we choose the measurement-to-spatial domain mapping $\mathcal{R}$ as Tikhonov regularisation

$$\mathcal{R}(\boldsymbol{M}_\lambda) = \boldsymbol{\Sigma}\boldsymbol{H}^\top \left(\boldsymbol{H}\boldsymbol{\Sigma}\boldsymbol{H}^\top + \boldsymbol{\Gamma}\right)^{-1} \boldsymbol{M}_\lambda, \tag{4}$$

where $\boldsymbol{\Sigma} \in \mathbb{R}^{N_x \times N_x}$ represents the slice covariance, and $\boldsymbol{\Gamma} \in \mathbb{R}^{K \times K}$ the measurement covariance. The Tikhonov step, which can be interpreted as noise whitening, was found to enable the downstream neural network to generalise more effectively to unseen noise levels (see [42]). The computation of covariances $\boldsymbol{\Sigma}$ and $\boldsymbol{\Gamma}$ is described in Section 8 of Supplementary document. Note that, as stated by Eq. (4), the Tikhonov regularisation applies to the transverse x-axis only, while the neural network $\mathcal{G}$ applies to both the transverse x- and longitudinal y- axis. The image domain neural network $\mathcal{G}_\theta$, is trained end-to-end in a supervised manner, i.e.,

$$\hat{\theta} \in \operatorname*{argmin}_{\theta} \frac{1}{L} \sum_{\ell} \|\mathcal{R}_\theta(\boldsymbol{M}^\ell) - \boldsymbol{F}^\ell\|_{\mathrm{F}}^2, \tag{5}$$

where $\{\boldsymbol{F}^\ell, \boldsymbol{M}^\ell\}$, $1 \leq \ell \leq L$, is a database of L image-measurement pairs and $\|\cdot\|_{\mathrm{F}}^2$ denotes the Frobenius norm. Please note that the reconstruction network only operates in the spatial domain, not the spectral domain. This is to minimise reconstruction biases that could be detrimental to the subsequent unmixing step. Furthermore, general databases are used for training, such as ImageNet (see Section 3.5), to prevent overfitting and ensure broad applicability to any samples.

3.4. Spectral unmixing: non-negative least squares

We formalise spectral unmixing as the constrained least squares minimisation problem

$$\operatorname*{argmin}_{\boldsymbol{A} \in \Omega} \|\hat{\boldsymbol{F}} - \boldsymbol{S}\boldsymbol{A}\|_{\mathrm{F}}^2, \tag{6}$$

where $\hat{\boldsymbol{F}} = [\hat{\mathcal{R}}(\boldsymbol{M}_1), \ldots, \hat{\mathcal{R}}(\boldsymbol{M}_\Lambda)]$ is the hypercube obtained after spatial reconstruction (see Section 3.3) and $\Omega \in \mathbb{R}^{Q \times N}$ represents the solution space. In the unconstrained case $\Omega = \mathbb{R}^{Q \times N}$, the solution is given by the pseudo inverse $\hat{\boldsymbol{A}} = (\boldsymbol{S}^\top \boldsymbol{S})^{-1} \boldsymbol{S}^\top \hat{\boldsymbol{F}}$, while the non-negative case $\Omega = \mathbb{R}_+^{Q \times N}$ requires an iterative algorithm such as [43]. Here, we assume that the spectral signatures $\boldsymbol{S}$ are known, which is the case for transgenic samples that express specific fluorescent proteins. The spectrum of autofluorescence may vary significantly across samples; however, it can be estimated from pure pixels, e.g., anatomical structures where no fluorescent proteins are present. The minimisation problem of Eq. (6) is solved using the `NNLS` function of the PySptools package.

3.5. Implementation details

In practice, we consider a sequence of $K = 128$ Hadamard patterns. We independently measure the positive components of the patterns, denoted by $\boldsymbol{H}^{+}$, and the negative components of the patterns, denoted by $\boldsymbol{H}^{-}$, where $\boldsymbol{H} = \boldsymbol{H}^{+} - \boldsymbol{H}^{-}$ is a Hadamard matrix (see Section 3 of Supplementary document). The raw measurements $\boldsymbol{M}^{+}$ and $\boldsymbol{M}^{-}$, acquired with $\boldsymbol{H}^{+}$ and $\boldsymbol{H}^{-}$, respectively, are binned to $\Lambda = 128$ spectral channels and $N_y = 512$ pixels in the longitudinal direction. After preprocessing (see Section 7 of Supplementary document), all Λ spectral slices are reconstructed using the Tikhonov-Net given by Eq. (3), where we choose the neural network $\mathcal{G}$ as a U-Net with $499,985$ trainable parameters and the Tikhonov solution given by $\mathcal{R}$ is computed using the actual patterns measured experimentally. The Tikhonov-Net has been integrated to SPyRiT, a python package dedicated to single-pixel imaging [44] that is based on PyTorch [45]. It is trained in an end-to-end fashion from simulations considering raw data corrupted by Poisson noise with an image intensity α of 50 photons. We consider the Adam optimiser for 20 epochs, with an initial step size of 10^{-3} that we divide by a factor of 2 every 10 epochs. We set the weight decay regularisation parameter to 10^{-7}. Our training database corresponds to the test set of the ImageNet ILSVRC2012 [46] where each of the 100k images is resized to $N_x \times N_y = 512 \times 512$. After spatial reconstruction, we compensate for a small spectral shift that is observed to vary linearly with the wavelength across the longitudinal dimension y.

4. Results

4.1. Spatial resolution of the imaging system

To characterise the spatial resolution of our device, we imaged an agarose solution containing fluorescent microspheres. The solution contains red and yellow-green fluorescent microspheres with a diameter of approximately 300 nm (Duke Scientific Polymer R300 Microspheres 0.3 µm and Polysciences Inc. Fluoresbrite® YG Microspheres 0.3 µm, both from Thermofisher®). The image obtained with the grayscale arm is shown in Fig. 2a, while that obtained with the hyperspectral imaging arm is shown Fig. 2d. We reconstruct the hypersectral image by inversion of Eq. (1) in the least squares sense (pseudoinverse). This constitutes the intrinsic resolution of the system, without any prior knowledge about the solution. For comparison purposes, we integrate the hyperspectral image over the spectral dimension. We selected two beads with the smallest spatial extent among all beads and clusters of beads observed in the field of view. In Fig. 2b–c and e–f, we plot the profiles across the centres of the beads. We estimate the spatial resolution along the x- and y-axis by measuring the FWHM of the profiles in the corresponding direction. In the case of the conventional image, we measure a resolution of 4 µm in both directions. In the case of the hyperspectral image, we measure a resolution of 15 and 7 µm along the x- and y-axis, respectively. Comparing the hyperspectral and grayscale arm, we observe a similar resolution along the y-axis, while the spatial resolution of the hyperspectral arm is 3 times greater than that of the grayscale arm along the x-axis (modulated dimension). We have also evaluated the spatial resolution of the hyperspectral arm for different numbers of patterns (see Table 1). We observe that the x-axis resolution depends linearly on the number of patterns, while the y-axis resolutions remains constant.

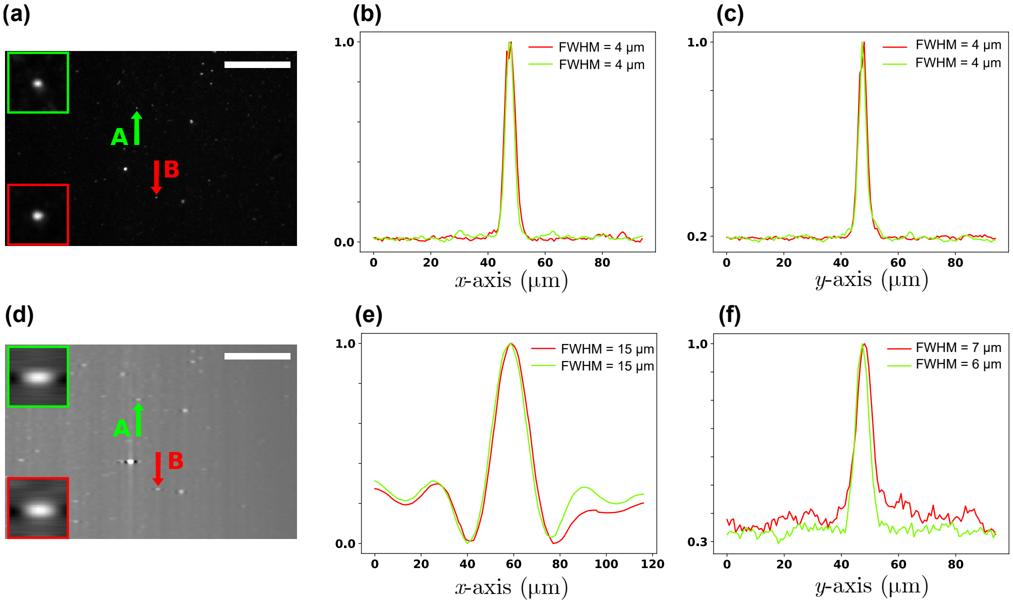

Fig. 2. Spatial resolution of the grayscale and hyperspectral arms. We image an agarose solution containing fluorescent microspheres using (a) the grayscale arm and (d) the hyperspectral arm using 128 patterns. We integrate the hyperspectral image over the spectral dimension. We select two beads (labelled 'A' and 'B' and indicated with arrows in (a) and (d)). The red and green boxes show the beads A and B magnified 4 times. Scale bars represent 100 µm. We plot the intensity profiles across the centre of the beads in the x- and y-direction for (b,c) the grayscale arm and (e,f) the hyperspectral arm.

Table 1. Spatial resolution of the hyperspectral arm as a function of number of patterns. Profiles analysed across the 'A' bead.

Number of patterns K	32	64	128
x-axis resolution (in µm)	77	36	15
y-axis resolution (in µm)	6	6	6

4.2. *Transgenic lines and sample preparation*

We imaged two transgenic zebrafish larvas: a Tg(fli1:EGFP; olig2:DsRed) larva and a Tg(sox10:mRFP; olig2:DsRed) larva. To obtain the double transgenic lines used in this study, the Tg(olig2:DsRed) fish were outcrossed with Tg(fli1:EGFP);Casper or Tg(sox10:mRFP) fish. The resulting Tg(fli1:EGFP);Casper;Tg(olig2:DsRed) and Tg(sox10:mRFP); Tg(olig2:DsRed) transgenic embryos were collected and raised under standard conditions according to the European Directive 2010/63/EU. The Tg(fli1:EGFP), Tg(olig2:DsRed) and Tg(sox10:mRFP) lines were produced at the zebrafish PRECI facility (Plateau de Recherche Expérimentale de Criblage In vivo, SFR Biosciences UAR3444/CNRS, US8/Inserm, ENS de Lyon, UCBL) in compliance with French government guidelines (agreement number C693870602). Developmental stages are given in days post-fertilization (dpf) at 28.5°C, based on morphological criteria as previously described [2]. At 1 dpf, the embryos were treated with 0.2 mM 1-phenyl 2-thiourea (Sigma-Aldrich, France) to inhibit pigmentation. Larvae were selected based on the expression of the fluorescent proteins of interest. They were sacrificed by an overdose of anaesthetic (0.2 % Tricaine, pH 7.0) and fixed at 4-5 dpf in paraformaldehyde for 2h at room temperature. After fixation, they were washed in PBDTT (1X PBS, 1% DMSO, 0.1% Tween, 0.5% Triton; all reagents from Sigma-Aldrich, France). The samples were then placed in spectrophotometer quartz cells and embedded in 1% low melting agarose (ThermoFisher Scientific, France), or mounted on a coverslip in DAKO mouting medium using a spacer for confocal acquisition. The samples were immediately used for observation or stored at 4-5°C in the dark before observation. Confocal images were acquired with an LSM 780 and LSM 800 microscope (Zeiss, Germany). The confocal images were formatted using the ‘Z projection’ tool in the Fiji software for confocal images.

4.3. Fellgett’s advantage and Tikhonov-Net reconstruction

The first hyperspectral light sheet microscope involved scanning an illumination line within the imaging plane [9], known as push-broom scanning in hyperspectral literature. Here, we propose the illumination of multiple lines at the same time to benefit from the signal-to-noise ratio improvement provided by multiplexed acquisitions [40]. To verify this improvement experimentally, we imaged a Tg(sox10:mRFP); Tg(olig2:DsRed) transgenic embryo using push-broom patterns and Hadamard patterns (see Fig. 3). We consider $K = 64$ push-broom patterns and $K = 64$ Hadamard patterns with positive and negative components measured independently. The integration time is set to 8 s for push-broom patterns and 4 s for Hadamard patterns, resulting in a total acquisition time of 512 s for both cases. The hyperspectral images reconstructed at 510, 551 and 594 nm are shown in Fig. 3. In the first and second row of Fig. 3, we reconstruct the images by inversion of Eq. (1) in the least squares sense, i.e., $\boldsymbol{F}_\lambda = \boldsymbol{H}^\dagger \boldsymbol{M}_\lambda$, where $\boldsymbol{H}^\dagger$ represents the pseudoinverse of the acquisition matrix measured for the push-broom patterns and for the Hadamard patterns, respectively.

We confirm that Hadamard patterns provide improved image quality across all wavelengths investigated. Felgett’s advantage appears more evident at low counts compared to high counts (compare images at 510 nm, where the lowest signal is obtained, and at 551 nm where the highest signal is measured). To quantify Felgett’s advantage, we computed the peak signal-to-noise ratio at each wavelength by dividing the maximum intensity by the standard deviation in a background region where no fluorescence is observed (see red rectangle on the top left image). We observe an improvement of 9.1, 7.8, and 7.9 dB at 510, 551 and 594 nm, respectively.

In the third row of Fig. 3, we reconstruct the same Hadamard measurements as in the second column using Tikhonov regularisation (i.e., Eq. (4)) and, in the fourth row of Fig. 3, using Tikhonov-Net (i.e., Eq. (3)) . Compared to pseudoinverse reconstructions, images obtained from Tikhonov regularisation are visually smoother and more contrasted, albeit exhibiting lower peak signal-to-noise ratios. We recall that the Tikhonov step can be interpreted as noise whitening, a property that enables the same convolutional neural network to perform well on spectral bins with varying signal-to-noise ratios (see [42]). Images reconstructed by Tikhonov-Net consistently yield the best peak signal-to-noise ratios and reveal more details, irrespective of the spectral bin.

4.4. Autofluorescence removal

We demonstrate quantitative imaging with autofluorescence removal in a 4-day-old Tg(fli1:EGFP; olig2:DsRed) zebrafish larva (Fig. 4). This fluorescent transgenic reporter line specifically expresses the fluorescent proteins EGFP (Enhanced Green Fluorescent Protein) and DsRed (Discosoma sp Red fluorescent protein) under the control of fli and olig2 promoters, respectively. The EGFP and DsRed emission peaks are well separated ($\Delta\lambda_{\mathrm{em}} \approx 80$ nm, see Fig. 4j) but suffer from autofluorescence. Figure 4a presents the conventional LSFM image acquired using the grayscale arm, while Fig. 4i,k present colour images acquired using a commercial confocal microscope (Zeiss LSM780) using two excitation wavelengths ($\lambda^{\mathrm{ex}}_{\mathrm{EGFP}} = 488$ nm and $\lambda^{\mathrm{ex}}_{\mathrm{DsRed}} = 561$ nm) and appropriate filters.

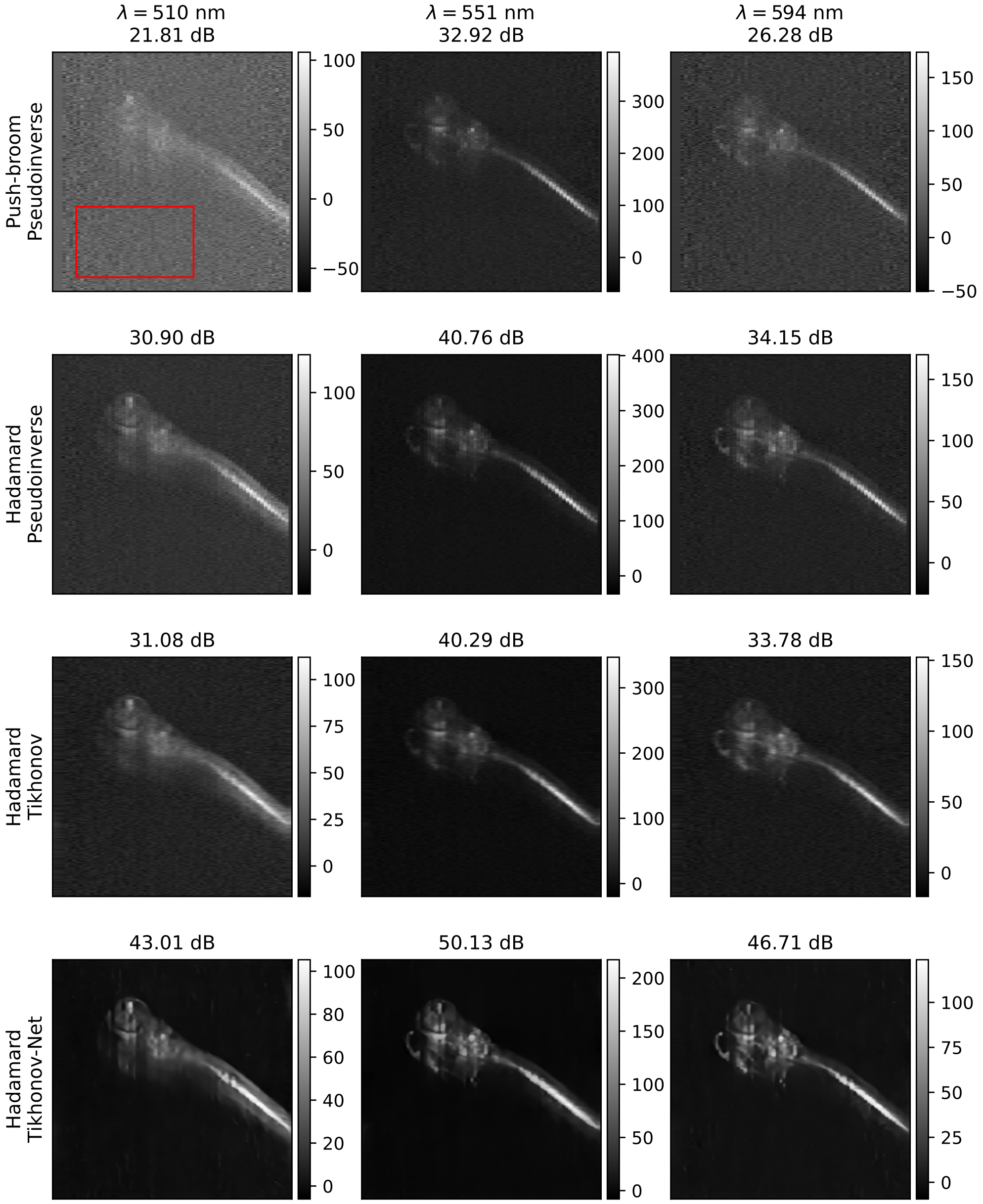

Fig. 3. Spectral images from push-broom and Hadamard acquisitions for several reconstruction methods. We reconstruct the image using: **First row**, the pseudoinverse of the push-broom patterns; **Second row**, the pseudoinverse of the Hadamard patterns; **Third row**, Tikhonov regularisation (i.e., Eq. (4)); **Fourth row**, Tikhonov-Net (i.e., Eq. (3)). We display the images at three central wavelengths: **First column**, 510 nm; **Second column**, 551 nm; **Third column**, 594 nm. Above each image, we display the peak signal-to-noise ratio computed within the red rectangle visible on the top left image. We acquire $N = 64$ push-broom patterns and $N = 64$ Hadamard patterns with positive and negative components measured independently. The integration time is set to 8 s for push-broom patterns and 4 s for Hadamard patterns, resulting in a total acquisition time of 512 s for both cases. The colour bars indicate the photon counts, which vary across images. The sample is a 4-day-old Tg(sox10:mRFP;olig2:DsRed) zebrafish larva (see Section 4.2).

Figure 4g–h show the EGFP and DsRed images obtained by conventional LSFM, filtered using two virtual band-pass filters whose spectral responses (Fig. 4j) were chosen to optimise the separation of the two fluorophores while minimising autofluorescence. Fluorescence is notably observed in the yolk sac of both images (Fig. 4g–h), a region where neither fli1 nor olig2 are expressed (fli1 is expressed in the vascular system [47], olig2 in the central nervous system [48]), which thus clearly indicates that filtering does not enable the removal of autofluorescence.

Figure 4d-f show the quantitative abundance maps for EGFP, DsRed and autofluorescence obtained by DNR-HLSFM. The spectral signature of EGFP and DsRed used for spectral unmixing have been taken from the Fluorescent Protein Database [49], while autofluorescence spectrum has been obtained from the yolk sac (Fig. 4a). Before unmixing, the notch filter is applied to the emission spectrum of EGFP and DsRed (see Fig. 4j). The EGFP abundance map (Fig. 4d) shows the endothelial cells that are present in the entire vasculature, in particular in the intersegmental vessels in the trunk and head, while the DsRed abundance map (Fig. 4e) shows the neural progenitors and oligodendrocytes that are present in the brain, retina and spinal cord, confirming the effectiveness of our approach. Furthermore, the autofluorescence abundance map (Fig. 4f) reveals that distribution is not uniform and consequently, that autofluorescence correction based on the conventional LSFM filter-based approach is inaccurate.

Figure 4b-c show the sample in, respectively, 2D and 3D after autofluorescence removal, obtained from the EGFP and DsRed quantitative abundance maps. The 3D images (Fig. 4c) represents 25 adjacent slices resulting in $512 \times 512 \times 25$ voxels of size $3 \times 3 \times 15$ µm^3, enhancing the structural and molecular understanding of the sample. The quantitative abundance maps and conventional LFSM images of the different slices are displayed in Fig. S7 and Fig. S8 of Supplementary document, respectively.

4.5. Separation of overlapping fluorophores

We demonstrate the spectral separation of two red fluorescent proteins in a 4-day-old Tg(sox10:mRFP; olig2:DsRed) zebrafish larva (see Fig. 5). Olig2 is expressed in the central nervous system, in particular the spinal cord [48], while sox10 is expressed in the neural cell and in the neural crest-derived Schwann cells located in the peripheral nervous system [50]. Separating sox10 from olig2 is particularly challenging due to the spectral overlap of the emission spectra of mRFP (monomeric Red Fluorescent Protein) and DsRed ($\Delta\lambda_{\text{em}} \approx 20$ nm, see Fig. 5j), as well as the spatial overlap of the sox10 and olig2 signal in the head and neural tube.

Figure 5a presents the conventional LSFM image acquired with the grayscale arm, while Fig. 5b–c present quantitative abundance maps of mRPF and DsRed (one slice of the sample in b, 3D representation in c) obtained by DNR-HLSFM. Figure 5i,k show the images obtained using a confocal microscope (Zeiss LSM780, $\lambda^{\text{ex}} = 561$ nm). Figure 5g–h show the images obtained by filtering conventional LSFM with two band-pass filters whose spectral responses were chosen to optimise the separation of mRFP and DsRed (see Fig. 5j). Despite these efforts, the mRFP and DsRed filtered images (Fig. 5g–h) are highly correlated, indicating significant overlap between the two fluorophores. More specifically, the mRFP image exhibits high intensity in the spinal cord, confirming that the filtering strategy fails to separate mRFP from DsRed. Figure 5d–f show the mRFP, DsRed and autofluorescence quantitative abundance maps obtained by DNR-HLSFM. The spectral signatures of mRFP and DsRed used for unmixing have been taken from the Fluorescent Protein Database [49], while that of autofluorescence has been measured in the yolk sac (see spectra in Fig. 5j).

By exploiting the full spectrum, the DNR-HLSFM pipeline successfully separates mRFP from DsRed despite their overlapping spectra. In the quantitative abundance maps, the mRFP signal is only observed in the neural crest cells in the brain (see Fig. 5d), while DsRed concentrates in the brain, retina and spinal cord (see Fig. 5e), confirming the effectiveness of our approach. Considering the cerebellum, in which olig2 is specifically expressed, this structure can be

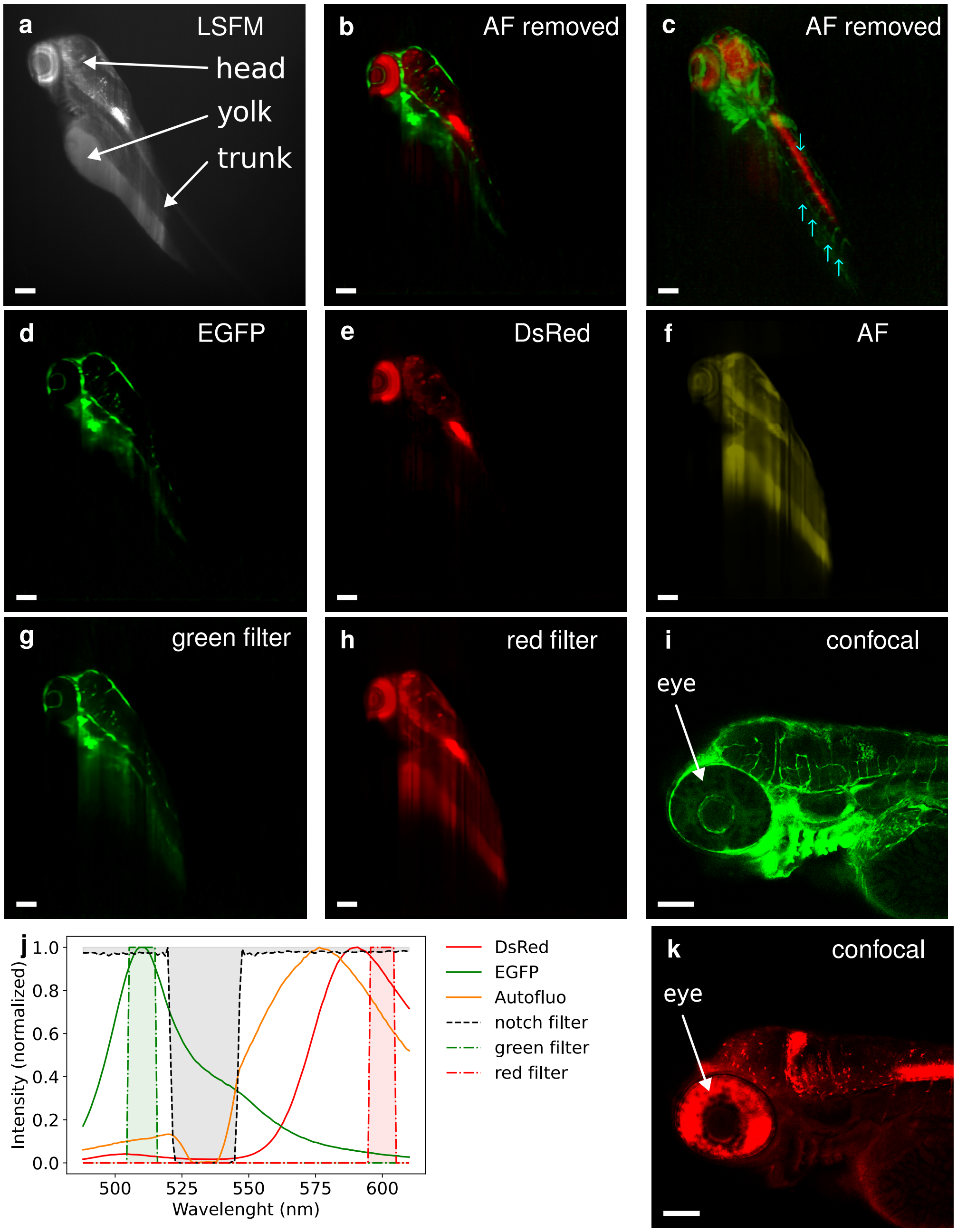

Fig. 4. Autofluorescence removal in a 4-day-old Tg(fli1:EGFP;olig2:DsRed) zebrafish larva. **a**, Conventional LSFM image acquired using the grayscale arm. **b–f**, Quantitative abundance maps obtained from DNR-HLSFM. **b–c**, Images after autofluorescence (AF) removal showing only the abundance of EGFP (in green) and DsRed (in red); **b** is the same slice as in **a**; **c** is the 3D representation obtained from 25 slices. (↓) points to the spinal cord, (↑) indicate the intersegmental vessels. **d–f**, Quantitative abundance maps of EGFP, DsRed and autofluorescence (AF) obtained using the spectra in **j** for unmixing; Superposing **d** and **e** leads to **b**. **g–h**, Images of EGFP and DsRed obtained by conventional LSFM, filtered using the two band-pass filters in **j**. **i,k**, Head of the embryo imaged by a commercial confocal microscope (Zeiss LSM780 using optical filters. **j**, Filters (dashed lines) and fluorescence spectra for spectral unmixing (solid lines). Lateral views, anterior is left. Scale bars = 100 µm.

observed in both the mRFP and DsRed images obtained by filtered conventional LSFM (Fig. 5.g-h). Conversely, the cerebellum is visible only in the DsRed and not mRFP quantitative abundance maps acquired using the hyperspectral structured LSFM pipeline (Fig. 5.d-e). Similarly to the previous example, the autofluorescence abundance map is found to vary spatially (see Fig. 5f), indicating that the conventional LSFM filter-based approach is inaccurate. It should be noted, however, that the concentration of autofluorescence around the spinal cord (see Fig. 5f) may be due to unmixing inaccuracies.

Figure 5c shows the distribution of DsRed and mRFP in 3D, obtained from the quantitative abundance maps of 20 adjacent slices resulting in $512 \times 512 \times 20$ voxels of size $3 \times 3 \times 15$ µm^3. The quantitative abundance maps and conventional LFSM images of the different slices are displayed in Fig. S9 and Fig. S10 of Supplementary document, respectively.

5. Discussion

We have demonstrated hyperspectral LSFM by shaping structured light sheets using only a DMD. Our optical system is simple, with no moving parts, few optical elements and does not require fast cameras. It can be combined with any standard filter-based light sheet microscopes. While LSFM is dominated by grayscale imaging, the palette of genetically encoded and synthesized fluorophores has enabled the labelling and observation of a large and constantly expanding number of molecular species [51]. Hyperspectral imaging offers the possibility of studying multiple components, cellular behaviours and cellular metabolism within the same specimen. In [9], the authors achieved hyperspectral imaging based on pushbroom acquisitions. Illuminating only a line of the imaging plane at a time, however, reduces light throughput compared to DNR-HLSFM which illuminates approximately half of the imaging plane at a time. The higher throughput of DNR-HLSFM translates into the so-called Fellgett's advantage [36]. Achieving line scan with our DMD-based device, we have have quantified an improved signal-to-noise of about 8 dB (see Section 4.3). The source intensity of a line scan can be increased to achieve the same amount of fluorescence emission as a Hadamard scan (e.g. by a factor of 128 for a Hadamard scan of order 128). However, this would result in a higher peak intensity for the line scan. This can be detrimental to the sample as photobleaching and phototoxic effects are highly nonlinear with respect to the excitation intensity [52]. Further studies should address this issue.

Hyperspectral alternatives based on tunable filers reject a large fraction of the fluorescent signal emitted by the sample [53], leading to poor light collection and increased photobleaching compared to DNR-HLSFM that exploits all emitted fluorescence photons. The snapshot imager introduced in [10] is fast but imposes a tradeoff between the field of view and the spectral resolution, whereas DNR-HLSFM, though slower due to is sequential nature, offers higher spectral resolution (e.g., <4 µm) over a larger field of view (e.g., 1.5×1.5 mm^2). The spectral resolution is determined by the focal length of the cylindrical lens, the slit width and the grating of the spectrometer. Raw acquisitions include 2,048 spectral channels that we have binned to 128 channels to match the spectral resolution of the spectrometer (2 nm, achieved with a 600 µm slit). We have chosen the largest slit available in order to maximise light throughput while ensuring the different fluorophores can be resolved.

While the longitudinal resolution along the slit of the spectrometer depends only on the collection objective, the transverse resolution transverse to the slit of the spectrometer is limited by the number of patterns displayed on the DMD and our ability to engineer systems capable of generating high-frequency structured light sheets. Using a collection objective with a low numerical aperture (NA = 0.1, at 500 nm theoretical Rayleigh resolution of ~3 µm and focal depth of ~50 µm), we have achieved a lateral resolution of 7 µm for a longitudinal resolution of 15 µm using 128 patterns (see Section 4.1) over a field of view of 1.5 mm^2. Higher spatial resolutions could be achieved using collection objectives with higher numerical aperture. Moreover, it has been shown that structured illumination LSFM can achieve resolutions below 100 nm in the

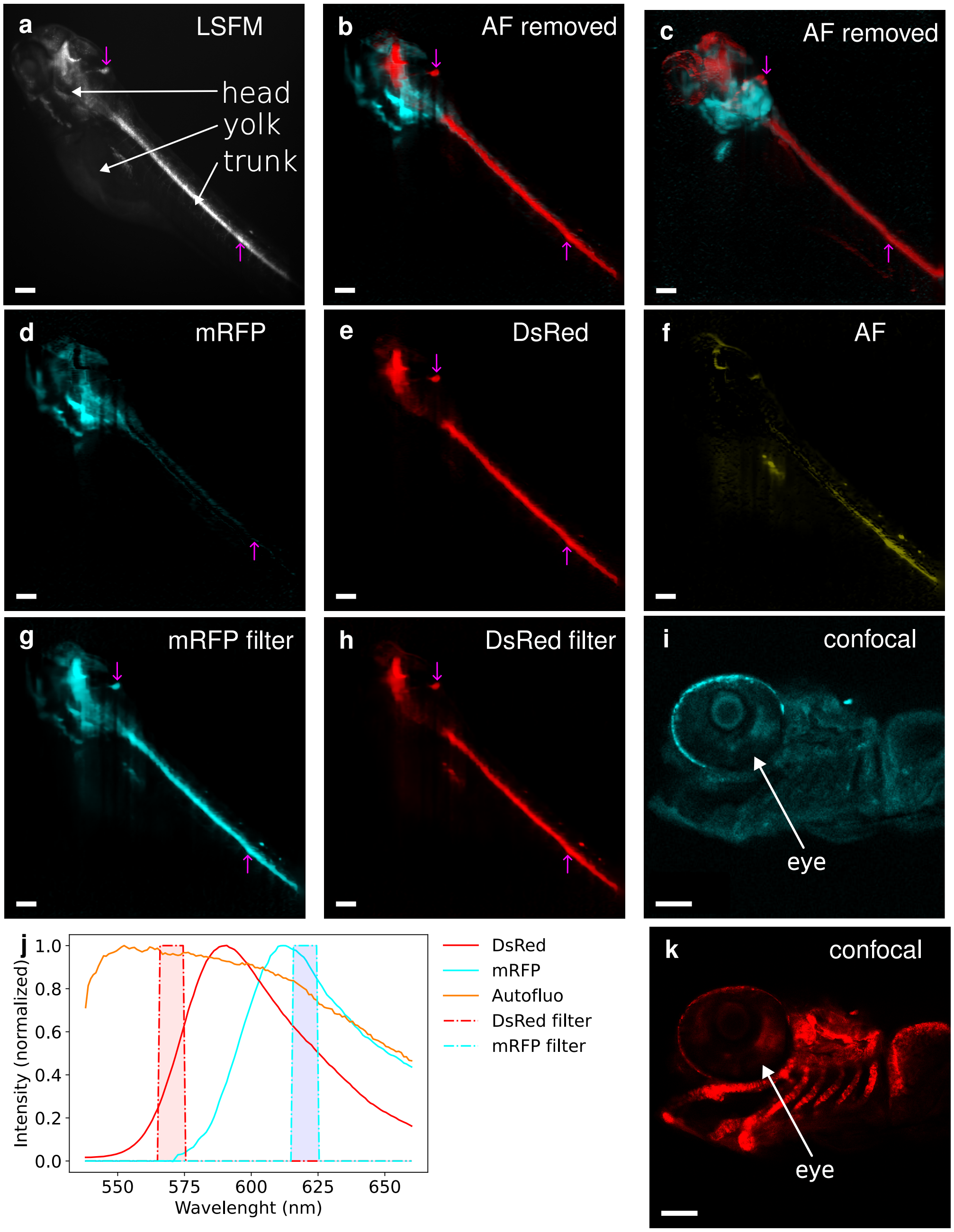

Fig. 5. Separation of fluorescent proteins with overlapping spectra. The sample is a 4-day-old Tg(sox10:mRFP;olig2:DsRed) zebrafish larva. **a–h**, Entire embryo imaged using conventional and DNR-HLSFM. **a**, Conventional LSFM image acquired using the grayscale arm. **b–c**, Quantitative abundance maps after autofluorescence (AF) removal obtained using DNR-HLSFM; **b** is the same slice as in **a**; **c** is the 3D representation obtained from 20 slices. **d–f**, Quantitative abundance maps of mRFP, DsRed and autofluorescence obtained by DNR-HLSFM using the spectra in **j** for unmixing. **g–h**, Images obtained by filtering conventional LSFM using the two band-pass filters whose response are depicted in **j**. **i,k**, Head of the embryo imaged by a commercial confocal microscope (Zeiss LSM780 using optical filters. **j**, Filters (dashed lines) and fluorescence spectra for spectral unmixing (solid lines).(↑) point to the spinal cord, (↓) indicate the cerebellum. Lateral views, anterior is left. Scale bars = 100 µm.

lateral direction [54], while random illuminations can also break the diffraction limit [55]. The spatial resolution of DNR-HLSFM is therefore ultimately limited by the number of patterns and light throughput, leading to a trade-off between the spatial resolution and the imaging speed in the longitudinal dimension. The spatial resolution could also be improved using software that incorporates the conventional LSFM images acquired using the grayscale arm, a technique known as pansharpening in remote sensing [56]. By shaping the light using a DMD, we can numerically adjust both the thickness of the light sheets and the transverse resolution, providing a high degree of flexibility to adapt to different samples.

Considering a power of 0.64 mW at the sample plane, DNR-HLSFM acquired more that $65,000 \times 128$ pixels (spatial × spectral) in approximately 8 min 30 s (see Table S2 of Supplementary document). The method in [9] achieved shorter acquisition times (down to 1.5 s) but with higher laser power (2–10 mW in the back focal plane of the illumination objective) and for only $2,000 \times 70$ pixels (spatial × spectral). For fair comparison, we introduce the power-time budget per pixel (see Section 4 of Supplementary document). The lower the power-time budget per pixel, the faster. While the pushbroom method in [9] works at ~200 µW.ms/pixel, DNR-HLSFM requires only 40–50 µW.ms/pixel (2–3 µW.ms/pixel before binning raw measurements), which constitutes an acceleration of one or two orders of magnitude. This analysis assumes a similar signal-to-noise ratio or image quality, which appears reasonable visually. However, further quantitative analysis is required to confirm this. It is also important to note that the acquisition of multiple slices has been done sequentially by translating the sample. The acquisition of multiple slices using DNR-HLSFM could be further accelerated by exploiting structured light sheets in the translation direction, in a similar fashion to [57–59], or even adapting the modulation to the sample, in line with the smart microscopy trend [60].

We have proposed a fast, simple yet effective, data-driven reconstruction method. Building on [42], our algorithm has only two steps. Alternatives include iterative algorithms based on the concept of unrolling [21] or plug-and-play [61] methods. The different spectral channels of the same hypercube have different intensities and hence different noise levels. It is therefore key to adapt regularisation to the noise level. In this regard, the Tikhonov step was found to generalise better to unseen noise levels than simpler alternatives based on the computation of the pseudo inverse solution, in accordance with previous studies [42]. Our approach reconstructs all spectral channels independently. More demanding alternatives could consider reconstruction strategies working across both the spatial and spectral dimensions, i.e., handling the different spectral channels jointly (e.g., see [62]). Here again, great care should be taken to avoid spectral distortions that would significantly degrade our ability to unmix the spectral components in the sample. The approach developed in [13] is fit-free and does not require any prior assumptions about the components. However, it assumes that a only few parameters are required to describe the measured spectra. Here, we have assumed that the emission spectra of the fluorescent proteins are known and constant across the sample, hence discarding spectral changes due to the local environment. However, the assumption may not be met in other samples. In this case, the spectra can be estimated together with the quantitative abundance maps. This problem, referred to as non-negative matrix factorisation, has a long history in statistics and linear algebra [63] but is much harder to solve.

6. Conclusion

Our work demonstrates that it is possible to achieve high-fidelity quantitative imaging in complex biological samples by combining structured illumination and data-driven hyperspectral unmixing techniques. Our approach eliminates the need for mechanical scanning. It results in increased light throughput compared to line scanning strategies and reduced photobleaching compared to filter-based approaches. We have experimentally validated our approach by successfully quantifying spectrally overlapping fluorophores and removing autofluorescence in zebrafish embryos, a widely used model in developmental biology and neuroscience. Fully computer-controlled, it opens up new horizons in biomedical research by enabling versatile strategies such as adaptive or smart scanning for fast and quantitative imaging. Future work will address samples with more fluorphophores, as well as increasing the spatial resolution and acquisition speed further.

Funding. Funding was received from the French National Research Agency (ANR-11-LABX-0063 and ANR-19-CE14-046) and the Institut universitaire de France (IUF).

Acknowledgements. S.C., C.R., and N.D. acknowledge support from Labex PRIMES (ANR-11-LABX-0063). N.D. acknowledges support from the Institut universitaire de France (IUF) and thanks Jérémy E. Cohen for insights on linear unmixing and non-negative matrix factorisation.

Data availability. Data underlying the results presented in this paper are available in [64], with the code available in [65]. Our database adheres to FAIR (Findability, Accessibility, Interoperability, Reusability) principles.

Disclosures. The authors declare no competing interests.

Supplemental document. See Supplement 1 for supporting content. The Supplemental document includes a description of the experimental setup, the handling of DMD diffraction, a characterisation of the light sheet, an analysis of the imaging speed of the system, the quantitative maps for all slices of the samples, the description of the noise model of the raw data, the description of the preprocessing of the raw data, and the description of the estimation of the covariance matrices.

References

1. J. Huisken and D. Y. R. Stainier, “Selective plane illumination microscopy techniques in developmental biology,” Development **136**, 1963–1975 (2009).
2. E. H. K. Stelzer, “Light-sheet fluorescence microscopy for quantitative biology,” Nat. Methods **12**, 23–26 (2015).
3. M. Weber and J. Huisken, “Light sheet microscopy for real-time developmental biology,” Curr. Opin. Genet. & Dev. **21**, 566–572 (2011).
4. O. E. Olarte, J. Andilla, E. J. Gualda, and P. Loza-Alvarez, “Light-sheet microscopy: A tutorial,” Adv. Opt. Photonics **10**, 111 (2018).
5. H. Kafian, S. Mozaffari-Jovin, M. Bagheri, and S. A. M. Shaegh, “Light-sheet fluorescent microscopy: Fundamentals, developments and applications,” Phys. Scripta **98**, 082001 (2023).
6. Y. Wan, K. McDole, and P. J. Keller, “Light-Sheet Microscopy and Its Potential for Understanding Developmental Processes,” Annu. Rev. Cell Dev. Biol. **35**, 655–681 (2019).
7. M. Dickinson, G. Bearman, S. Tille, et al., “Multi-Spectral Imaging and Linear Unmixing Add a Whole New Dimension to Laser Scanning Fluorescence Microscopy,” BioTechniques **31**, 1272–1278 (2001).
8. G. Lu and B. Fei, “Medical hyperspectral imaging: A review,” J. Biomed. Opt. **19**, 010901 (2014).
9. W. Jahr, B. Schmid, C. Schmied, et al., “Hyperspectral light sheet microscopy,” Nat. Commun. **6**, 7990 (2015).
10. Z. Lavagnino, J. Dwight, A. Ustione, et al., “Snapshot Hyperspectral Light-Sheet Imaging of Signal Transduction in Live Pancreatic Islets.” Biophys. journal **111**, 409–417 (2016).
11. I. Rocha-Mendoza, J. Licea-Rodriguez, M. Marro, et al., “Rapid spontaneous Raman light sheet microscopy using cw-lasers and tunable filters,” Biomed. Opt. Express **6**, 3449–3461 (2015).
12. W. Müller, M. Kielhorn, M. Schmitt, et al., “Light sheet Raman micro-spectroscopy,” Optica **3**, 452–457 (2016).
13. P. N. Hedde, R. Cinco, L. Malacrida, et al., “Phasor-based hyperspectral snapshot microscopy allows fast imaging of live, three-dimensional tissues for biomedical applications,” Commun. Biol. **4**, 1–11 (2021).
14. S. Crombez, P. Leclerc, C. Ray, and N. Ducros, “Computational hyperspectral light-sheet microscopy,” Opt. Express **30**, 4856–4866 (2022).
15. J. Morizet, D. Chow, P. Wijesinghe, et al., “UVA Hyperspectral Light-Sheet Microscopy for Volumetric Metabolic Imaging: Application to Preimplantation Embryo Development,” ACS Photonics **10**, 4177–4187 (2023).
16. P. Wang, M. Kitano, K. Keomanee-Dizon, et al., “A single-shot hyperspectral phasor camera for fast, multi-color fluorescence microscopy,” Cell Reports Methods **3**, 100441 (2023).
17. A. Dvornikov and E. Gratton, “Hyperspectral imaging in highly scattering media by the spectral phasor approach using two filters,” Biomed. Opt. Express **9**, 3503–3511 (2018).
18. E. J. Candes and M. B. Wakin, “An Introduction To Compressive Sampling,” IEEE Signal Process. Mag. **25**, 21–30 (2008).
19. S. Arridge, P. Maass, O. Öktem, and C.-B. Schönlieb, “Solving inverse problems using data-driven models,” Acta Numer. **28**, 1–174 (2019).
20. G. Barbastathis, A. Ozcan, and G. Situ, “On the use of deep learning for computational imaging,” Optica **6**, 921–943 (2019).

21. V. Monga, Y. Li, and Y. C. Eldar, "Algorithm Unrolling: Interpretable, Efficient Deep Learning for Signal and Image Processing," IEEE Signal Process. Mag. **38**, 18–44 (2021).
22. J. Zhang, B. Chen, R. Xiong, and Y. Zhang, "Physics-Inspired Compressive Sensing: Beyond deep unrolling," IEEE Signal Process. Mag. **40**, 58–72 (2023).
23. D. Gedalin, Y. Oiknine, and A. Stern, "DeepCubeNet: Reconstruction of spectrally compressive sensed hyperspectral images with deep neural networks," Opt. Express **27**, 35811–35822 (2019).
24. S.-H. Baek, H. Ikoma, D. S. Jeon, et al., "End-to-End Hyperspectral-Depth Imaging with Learned Diffractive Optics," arXiv:2009.00463 [cs, eess] (2020).
25. M. Yako, Y. Yamaoka, T. Kiyohara, et al., "Video-rate hyperspectral camera based on a CMOS-compatible random array of Fabry–Pérot filters," Nat. Photonics **17**, 218–223 (2023).
26. L. Huang, R. Luo, X. Liu, and X. Hao, "Spectral imaging with deep learning," Light. Sci. & Appl. **11**, 61 (2022).
27. Y. Xu, L. Lu, V. Saragadam, and K. F. Kelly, "A compressive hyperspectral video imaging system using a single-pixel detector," Nat. Commun. **15**, 1456 (2024).
28. J. Wen, H. Gao, W. Shi, et al., "Real-time Hyperspectral Imager with High Spatial-Spectral Resolution Enabled by Massively Parallel Neural Network," ACS Photonics **12**, 1448–1460 (2025).
29. C. Zhang, X. Liu, L. Wang, et al., "Lensless efficient snapshot hyperspectral imaging using dynamic phase modulation," Photonics Res. **13**, 511–526 (2025).
30. Q. Xue, Y. Yang, W. Ma, et al., "Advances in Miniaturized Computational Spectrometers," Adv. Sci. **11**, 2404448 (2024).
31. Y. Zhang, L. Zhang, Y. Zhu, et al., "High-Spatial and Spectral Resolution Snapshot Spectral Imaging Based on Nearfield Coupled Metasurfaces," ACS Photonics (2025).
32. M. Duarte, M. Davenport, D. Takhar, et al., "Single-Pixel Imaging via Compressive Sampling," Signal Process. Mag. IEEE **25**, 83–91 (2008).
33. Z. Zhang, X. Ma, and J. Zhong, "Single-pixel imaging by means of Fourier spectrum acquisition," Nat. Commun. **6**, 6225 (2015).
34. E. Hahamovich, S. Monin, Y. Hazan, and A. Rosenthal, "Single pixel imaging at megahertz switching rates via cyclic Hadamard masks," Nat. Commun. **12**, 4516 (2021).
35. X. Zhang, C. Deng, C. Wang, et al., "VGenNet: Variable Generative Prior Enhanced Single Pixel Imaging," ACS Photonics **10**, 2363–2373 (2023).
36. M. Harwit and N. J. A. Sloane, Hadamard Transform Optics (Academic Press, 1979).
37. P. B. Fellgett, "On the Ultimate Sensitivity and Practical Performance of Radiation Detectors," J. Opt. Soc. Am. **39**, 970 (1949).
38. C. Scotté, F. Galland, and H. Rigneault, "Photon-noise: Is a single-pixel camera better than point scanning? A signal-to-noise ratio analysis for Hadamard and Cosine positive modulation," J. Physics: Photonics **5**, 035003 (2023).
39. R. M. Power and J. Huisken, "A guide to light-sheet fluorescence microscopy for multiscale imaging," Nat. Methods **14**, 360–373 (2017).
40. N. J. A. Sloane and M. Harwit, "Masks for Hadamard transform optics, and weighing designs," Appl. Opt. **15**, 107–114 (1976).
41. S. Hariga, J. E. Cohen, and N. Ducros, "Joint Reconstruction and Spectral Unmixing from Single-Pixel Acquisitions," in 2024 32nd European Signal Processing Conference (EUSIPCO), (IEEE, Lyon, France, 2024), pp. 661–665.
42. A. Lorente Mur, P. Leclerc, F. Peyrin, and N. Ducros, "Single-pixel image reconstruction from experimental data using neural networks," Opt. Express **29**, 17097–17110 (2021).
43. R. Bro and S. De Jong, "A fast non-negativity-constrained least squares algorithm," J. Chemom. **11**, 393–401 (1997).
44. G. Beneti Martins, L. Mahieu-Williame, T. Baudier, and N. Ducros, "OpenSpyrit: An ecosystem for open single-pixel hyperspectral imaging," Opt. Express **31**, 15599 (2023).
45. A. Paszke, S. Gross, F. Massa, et al., "PyTorch: An imperative style, high-performance deep learning library," in Advances in Neural Information Processing Systems 32, H. Wallach, H. Larochelle, A. Beygelzimer, et al., eds. (Curran Associates, Inc., 2019), pp. 8024–8035.
46. O. Russakovsky, J. Deng, H. Su, et al., "ImageNet Large Scale Visual Recognition Challenge," Int. J. Comput. Vis. **115**, 211–252 (2015).
47. N. D. Lawson and B. M. Weinstein, "In Vivo Imaging of Embryonic Vascular Development Using Transgenic Zebrafish," Dev. Biol. **248**, 307–318 (2002).
48. L. Fontenas, T. G. Welsh, M. Piller, et al., "The Neuromodulator Adenosine Regulates Oligodendrocyte Migration at Motor Exit Point Transition Zones," Cell Reports **27**, 115–128.e5 (2019).
49. T. J. Lambert, "FPbase: A community-editable fluorescent protein database," Nat. Methods **16**, 277–278 (2019).
50. J. Kwak, O. K. Park, Y. J. Jung, et al., "Live Image Profiling of Neural Crest Lineages in Zebrafish Transgenic Lines," Mol. Cells **35**, 255–260 (2013).
51. K. Thorn, "Genetically encoded fluorescent tags," Mol. Biol. Cell **28**, 848–857 (2017).
52. J. Icha, M. Weber, J. C. Waters, and C. Norden, "Phototoxicity in live fluorescence microscopy, and how to avoid it," BioEssays **39**, 1700003 (2017).
53. B. Boldrini, W. Kessler, K. Rebner, and R. W. Kessler, "Hyperspectral Imaging: A Review of Best Practice, Performance and Pitfalls for in-line and on-line Applications," J. Near Infrared Spectrosc. **20**, 483–508 (2012).
54. B.-J. Chang, V. D. Perez Meza, and E. H. K. Stelzer, "csiLSFM combines light-sheet fluorescence microscopy and

coherent structured illumination for a lateral resolution below 100 nm," Proc. National Acad. Sci. **114**, 4869–4874 (2017).

55. L. Mazzella, T. Mangeat, G. Giroussens, et al., "Extended-depth of field random illumination microscopy, EDF-RIM, provides super-resolved projective imaging," Light. Sci. & Appl. **13**, 285 (2024).
56. L. Loncan, L. B. de Almeida, J. M. Bioucas-Dias, et al., "Hyperspectral Pansharpening: A Review," IEEE Geosci. Remote. Sens. Mag. **3**, 27–46 (2015).
57. G. Calisesi, M. Castriotta, A. Candeo, et al., "Spatially modulated illumination allows for light sheet fluorescence microscopy with an incoherent source and compressive sensing," Biomed. Opt. Express **10**, 5776–5788 (2019).
58. Y.-X. Ren, J. Wu, Q. T. K. Lai, et al., "Parallelized volumetric fluorescence microscopy with a reconfigurable coded incoherent light-sheet array," Light. Sci. & Appl. **9**, 8 (2020).
59. A. Zunino, F. Garzella, A. Trianni, et al., "Multiplane Encoded Light-Sheet Microscopy for Enhanced 3D Imaging," ACS Photonics **8**, 3385–3393 (2021).
60. S. Daetwyler and R. P. Fiolka, "Light-sheets and smart microscopy, an exciting future is dawning," Commun. Biol. **6**, 1–11 (2023).
61. K. Zhang, Y. Li, W. Zuo, et al., "Plug-and-Play Image Restoration With Deep Denoiser Prior," IEEE Trans. on Pattern Anal. Mach. Intell. **44**, 6360–6376 (2022).
62. V. Pronina, A. Lorente Mur, J. F. P. J. Abascal, et al., "3D denoised completion network for deep single-pixel reconstruction of hyperspectral images," Opt. Express **29**, 39559 (2021).
63. D. D. Lee and H. S. Seung, "Learning the parts of objects by non-negative matrix factorization," Nature **401**, 788–791 (1999).
64. "https://pilot-warehouse.creatis.insa-lyon.fr/#collection/63caa9497bef31845d991351," .
65. "https://github.com/openspyrit/spyrit-examples/tree/master/2025_hLSFM," .